AllSpark: Enabling Long-Range Backscatter for Vehicle-to-Infrastructure Communication

Xuan Wang, Xin Kou, Haoyu Li, Fuwei Wang, Dingyi Fang, *Member, IEEE*, Yunfei Ma, *Member, IEEE*, and Xiaojiang Chen, *Member, IEEE*

***Abstract*—Long-range backscatter communication has the potential to provide enough time and space for vehicles to detect traffic information, which is an attractive solution for Vehicle-to-Infrastructure (V2I) communication. However, existing backscatter studies either require the tag to be close to the carrier source (ambient backscatter) or have poor receiver sensitivity (RFID), making it challenging to satisfy the high range requirements of V2I communication. In this article, we develop AllSpark to investigate the feasibility of long-range communication enabling backscatter to be applied to V2I. Specifically, to increase RSS to compensate for the enormous dual-path loss in backscatter systems, we first redesign the tag's radio frequency (RF) front-end to amplify the incident signals, and then we design high-gain directional antennas for the tag and reader. Second, we present EC-Net, an end-to-end demodulator that selectively enhances signal features (denoising) and is tuned to lower classification (demodulation) error to maximize demodulation accuracy. Furthermore, we adopt convolutional encoding for tag data and use the output probability of EC-Net to design an effective soft decoder to resist occasional interference and noise, improving communication robustness. Our prototype and experiments outdoors verify the effectiveness of AllSpark which can provide a communication range of 700 m. Even in a moving scene, it can achieve a communication range of 600 m, demonstrating that AllSpark has the potential to be applied for autonomous driving and low-flying drones to detect traffic conditions.**

***Index Terms*—Backscatter, long-range, vehicle-to-infrastructure (V2I).**

I. Introduction

IDENTIFYING road and traffic conditions is critical for enhancing autonomous driving safety. However, commercial sensors installed in self-driving cars, such as cameras, infrared, and Lidar, will face a detecting disaster of false judgments or failure when traveling in adverse weather (e.g., fog, snow, rain, and haze). Since wireless signals have good penetration, reliable vehicle-to-infrastructure (V2I) communication [1], [2] provides an effective auxiliary solution for improving detection accuracy when the target is out of sight or has impaired vision. Among them, dedicated short-range communications (DSRC) [3] are the most mature technology applied. Although it can communicate over a distance of hundreds of meters or even one kilometer, the high cost (thousands of dollars) [4] and high power consumption (>1 W) [5] of road side unit (RSU) result in an extraordinarily high purchase and maintenance expenses when deployed at scale. For example, according to [4], if 20 RSUs are required to cover a 10-km road, the purchase price will be $26 000, with installation and configuration costs of around $57 000. In addition, because of its high power consumption (5 W) [6], each RSU requires an extra 9–30 V power supply, resulting in an annual maintenance cost of about $1000 per unit. Therefore, the low-power and low-cost V2I technology need to be investigated.

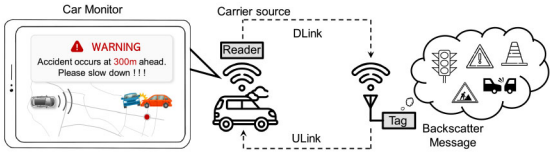

Fig. 1. Geometric topology of AllSpark.

The backscatter technology provides a potential solution for V2I applications since it uses orders of magnitude less power than active radio RSU. Fig. 1 displays a picturesque example. Backscatter tags with customized antennas are affixed to roadside infrastructures, such as temporarily parked cars, road construction sites, checkpoints, etc. When a reader-equipped vehicle approaches a tag, the tag modulates the reader's carrier signal to piggyback its information. The car then decodes the embedded data, which might warn the driver or control system to take action ahead of time. A detection distance of at least 600 m is required to be suitable for a practical application.

However, limited communication range has always been the bottleneck for low power backscatter, whether it is conventional RFID [7], [8], [9] or ambient backscatter (utilizing ambient environmental signals, such as WiFi [10], LTE [11], and TV [12]). There are two reasons: 1) due to power consumption constraints, the backscatter tag typically employs a low-sensitivity envelope detector, making it difficult to identify a weak carrier signal from a long-distance reader. The tag cannot be activated if the detection fails, resulting in a short downlink distance (reader to tag, DLink) and 2) the received signal power degrades as $1/R^4$ due to dual-path propagation loss from the reader to tag and from tag to the reader (R is the

Manuscript received 16 March 2022; revised 9 May 2022 and 3 July 2022; accepted 25 July 2022. Date of publication 19 August 2022; date of current version 7 December 2022. This work was supported in part by the National Natural Science Foundation of China (NSFC) under Grant 61972316 and Grant 61802309; in part by the International Cooperation Project of Shaanxi Province under Grant 2020KWZ-013; and in part by the Natural Science Foundation of Shaanxi Province under Grant 21JK0934. *(Corresponding author: Xiaojiang Chen.)*

Xuan Wang, Xin Kou, Haoyu Li, Fuwei Wang, Dingyi Fang, and Xiaojiang Chen are with the School of Information Science and Technology, Northwest University, Xi'an 710127, China, and also with the Shaanxi International Joint Research Centre for the Battery-Free Internet of Things, Xi'an, China (e-mail: xjchen@nwu.edu.cn).

Yunfei Ma is with the Network Research, Alibaba Group, Hangzhou 310052, China.

Digital Object Identifier 10.1109/JIOT.2022.3197596

distance between reader and tag), causing it to become weak and even drown in noise.

A large and growing body of literature has investigated increasing range [13], [14], [15], [16], [17], [18]. Nevertheless, they either need to synchronize multiple readers to beamform power to wake up tags or separate the transceiver so that the tag is close to the carrier source, which comes with a hefty deployment cost when used for V2I.

In this article, we propose AllSpark, a long-range backscatter system with only one transceiver to meet the highly challenging requirements of V2I communication. Through the investigation of hardware and software design, namely, the design of antennas, tag hardware, and digital end, we increase the communication range to 700 m. Below we describe the design of the three stages.

Antennas Design (Section V-A): We first design high-gain directional microstrip array antennas for the tag and the reader, respectively, which spatially focus the radiation energy on the dominant path while suppressing interference signals from undesired paths. The link gain is increased by 52 dB thanks to the antennas design.

Tag Hardware Design (Section V-B): Although received signal strength (RSS) has significantly improved, it still requires 28 dB to achieve our goal. Next, we increase link gain by providing a signal amplification module (SAM) design for the tag. This module improves the incident signals' signal-to-noise ratio (SNR) while wasting very little energy. The key challenge is to add a unidirectional amplifier to the backscatter tag, which has one radio frequency (RF) port for backscattering signals. Although a power splitter or RF tee connector can be used to separate the incident and backscatter links, allowing an amplifier to be added for the tag, the power will be blocked by half. To overcome this difficulty, we utilize the circulator's one-way transmission property to realize link separation and choose a low noise amplifier (LNA) to magnify the signal power. Our results show that SAM has a gain improvement of 26.2 dB.

Digital End (Section VI): Our above hardware design improves the RSS of the backscattered signal, which extends communication distance significantly. However, in wireless transmission, noise interference signals may substantially disturb useful signals, causing poor SNR at the reader and numerous errors. Although traditional denoising methods (such as wavelet and thresholding) can lessen noise, they also weaken useful signals, leading to a slight increase or even a little drop in SNR. The bit error rate (BER) will be more significant when demodulating from the de-noised signal. To resist noise, we present an EC-Net demodulator, deep learning (DL)-based demodulator framework (Section VI-A). EC-Net demodulator is jointly optimizing a classification model (demodulation) and signal enhancement model (denoising). It enables selectively enhancing the signal feature for maximizing classification accuracy, i.e., demodulation accuracy. This is in contrast to conventional demodulators that process denoising and demodulation separately. Furthermore, we encode the transmitted data via convolutional coding, which provides a superior coding gain with less resource consumption. We then introduce a soft decoder that offers higher error-correcting capabilities in noise and interference channels by utilizing the output probability of EC-Net rather than the final classification category (Section VI-B). Our digital design achieves 3.2 dB of extra SNR gain.

To sum up, the main contributions of this article can be summarized as follows.

1) We design AllSpark, a long-range backscatter communication system, which enables readers to communicate with tags even in the mobile scene. It meets the range requirement of V2I communication.
2) We adopt measures combined with hardware and software to improve the communication range significantly. On the one hand, we boost RSS by designing an SAM for tag and high gain microstrip array antennas for tag and reader. On the other hand, to reduce BER under low SNR, we design a DL demodulator framework EC-Net and a soft decoder for the reader to resist sudden interference and noise.
3) We built a prototype of AllSpark which contains an assembled tag with customized and off-the-shelf components, as well as a USRP software radio. We conducted extensive experiments in an RF shielding anechoic chamber and on an open road to evaluate the performance of AllSpark. The preliminary results demonstrate that it can provide a range of 700 m. Even in the case of the mobile reader, it has a communication range of 600 m, enabling real-world driving applications where vehicles must detect the road conditions ahead to have adequate space and time to respond. This system also provides ideas to ensure the safety of unmanned aerial vehicles (UAVs) flying at low altitudes in the future.

The remainder of this article is organized as follows. In Section II, related work is discussed. In Section III, we calculate the communication range required for V2I applications and determine how much extra gain is required to accomplish such a long range. We present the system overview of AllSpark in Section IV. In Section V, hardware design (antennas and tag) is described in detail, followed by the design of the EC-Net demodulator and our soft decoder in Section VI. The experimental evaluation is presented in Section VII. Finally, in Section VIII, conclusion and future work is discussed.

II. Related Work

Existing Wireless Backscatter Technology: The backscatter technology has been extensively researched for application in intelligent transportation systems [19], [20], [21], [22], [23], [24], [25] because of its advantages of low cost and low power consumption. In [24], readers deployed on roadside poles to locate the RF transponders mounted on the cars and measure their moving speed. The visible light backscatter communication technology also enables the battery-free tag to communicate with the visible light source passively [26], [27]. However, since harsh environments may significantly affect visible light, varying lighting leads to unreliable communication. The millimeter-wave backscatter technology can be compatible with existing vehicle-mounted millimeter-wave radar to complete the V2I collaboration [28], [29], [30], [31]. Millimetro [31] designed

an ultralow-power modulating mmWave backscatter tag that is compatible with commercial mmWave automotive radars. It achieves cm-level accuracy ranging over 100 m, a huge breakthrough for millimeter waves. However, the communication range of both works is not far enough. Although wireless backscatter has unique advantages in power consumption and computing overhead, the communication distance is greatly limited due to the passive nature of the backscatter tags. If the vehicle does not have enough range to communicate with tags, it is dangerous for high-speed driving.

Long-Range Backscatter Communication: Increasing backscatter range has recently become the subject of much research to accommodate a wide range of communication scenarios. For instance, Full-Duplex LoRa Backscatter [32] eliminates self-interference through hardware design at the reader, which improves the receiver's sensitivity and achieves a communication range of more than 90 m. The approaches separate the transceiver and place the tag close to either the ambient carrier generator or the receiver about centimeters to raise the distance to a few thousand meters [11], [18], [33]. The passive tag of PLoRa [33] has a backscatter range of 1.1 km when the tag is at a distance of 20 cm from the Lora node. Ambient backscatter [12] uses the TV signal as the carrier and the communication range between the transmitter and the tag, but the tag needs to be very close to the receiver. The other method uses negative resistance components such as the tunnel-diode on the tags to significantly increase the distance of the backscatter [34], [35], [36]. A backscatter tag based on a tunneling diode is designed in TunnelScatter [36] to overcome the limitation that the backscatter tag needs to be close to the carrier transmitter to receive a strong carrier signal. Tag data can be transmitted when there is no carrier signal or when the carrier signal strength is weak, significantly improving the communication range.

III. Requirements Analysis

Through two aspects: link budget and receiver sensitivity, this section examines how much link gain is required to satisfy the communication range requirement for V2I applications.

A. Link Budget for Backscatter System

The link budget analysis for our frequency-shift backscatter system can be modeled as bistatic collocated backscatter characterized detailed in [37]. Assume that there is no system loss during tag modulation and no multipath and interference in ideal circumstances. The total signal power received by the reader can be expressed as follows:

$$P_{Rx} = \frac{P_{Tx} G_{Tx} G_{\text{tag}}^2 G_{Rx}}{(4\pi)^4} \left(\frac{\lambda_1 \lambda_2}{r_1 r_2}\right)^2 \tag{1}$$

where P_T is transmitted signal power, G_T, G_R, and G_{tag} are load matched, free-space antenna gain of transmitter, receiver and tag, respectively, λ_1 is the wavelength of carrier signal and r_1 is the DLink distance from transmitter to tag. λ_2 is the wavelength of shifted backscattered signal and r_2 is the ULink distance from tag to receiver.

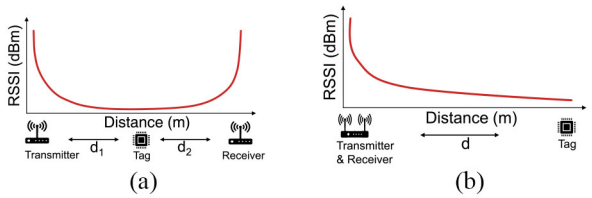

Fig. 2. Variation of RSS for bistatic dislocated and collocated deployments. (a) Bistatic dislocated. (b) Bistatic collocated.

For our bistatic collocated backscatter system, $r_1 = r_2$, the variation curve of P_{Rx} as distance increases is shown in Fig. 2(b), corresponding to the worst case in Fig. 2(a) where the tag is in the middle of the transmitter and receiver and the backscattered signal is the weakest.

Thus, how to increase the backscatter communication distance for collocated deployment is a complex problem since we have to increase both r_1 and r_2. Constraints of long-range naturally lead us to a solution that operates at the sub-GHz (RFID, 902–928 MHz) frequency bands since it has a low loss and better penetration characteristic.

B. Receiver Sensitivity

The other factor that determines communication range is receiver sensitivity, which can be expressed as follows:

$$\text{Noise Floor} = -174\text{dBm/Hz} + NF + 10\log B + \text{SNR}_{\text{min}}. \tag{2}$$

NF is Noise Figure, B is the signal's bandwidth, and SNR_{min} means the minimum SNR required for correct decoding. The higher the sensitivity, the longer the communication distance. We can further decrease the minimum SNR required for correct decoding to improve receiver sensitivity for a particular signal and Noise Figure.

C. Gain Improvement Requirement

Assuming that the maximum average transmits power is 33 dBm for 900 MHz, and USRP receiver sensitivity is -102 dBm. Given a tag has an ideal insertion loss of 3 dB and cable loss is 2 dB, there is a dynamic range of 33 dBm - (-102 dBm) -3 dB -2 dB $=$ 130 dB for signal propagation. For our deployment, the one-way loss is 65 dB, and the communication range can only achieve 45 m.

To be a practical V2I solution, there must be enough communication range to enable enhanced comfort for passengers while still assuring safe driving. Even worse, a slick road surface increases braking distance dramatically on rainy or snowy days. Based on braking speed and reaction time, we can estimate that the detection distance must be greater than 600 m in most situations to meet safe driving requirements.

Furthermore, the wireless channel is highly complex, with several barriers, resulting in uncertain multipath and fading. As a result, theoretical distance cannot be achieved in a practical setting. We deduct dual-path air loss of 30 dB (obtained from several measurements) from the free space transmission model (1) to make it compatible with the actual signal transmission. To summarize, another 75-dB gain must be raised to attain the desired communication range.

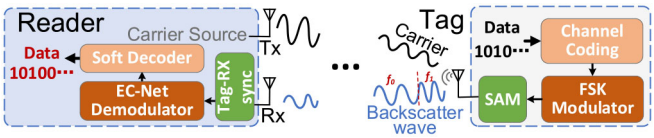

Fig. 3. Overview of AllSpark.

In the following sections, we explore two ways to attain a long and reliable communication distance. The first step is to increase RSS through antennas and tag hardware design. The second step is to raise receiver sensitivity by improving demodulation and decoding performance at low SNR.

IV. System Overview

We design a long-range backscatter communication system AllSpark, which explores a variety of approaches to satisfy the long-range requirement for V2I. Fig. 3 shows a high-level overview of AllSpark.

A. Reader

Similar to the conventional RFID, the reader contains one transmitter that generates an excitation carrier and a receiver that demodulates and decodes the backscattered data of the tag. The customized tag piggybacks the data it wants to send by FSK modulation. The remainder of this section describes these components.

B. Tag

To increase communication range significantly, we design a SAM for the tag to boost RSS. Furthermore, we adopt the FSK as lorea [18] recommended modulating and shifting the carrier by toggling RF switch with two frequencies. FSK has been shown to be able to obtain a lower BER for the same SNR than on-off keying (OOK) due to robustness against fading and noise, resulting in orders of magnitude improvement in communication range.

In order to increase robustness under low SNR further, we adopt convolution coding as the channel coding with anti-jamming and error-correcting capabilities by adding redundancy. We also discuss picking an appropriate coding rate in detail in Section VI-B.

V. Hardware Design for Increasing RSS to Improve Communication Range

This section focuses on improving communication range by increasing RSS. We first design high-gain microstrip array antennas for the reader and tag, respectively. Second, we design a tag with a SAM to increase the power of the incident and backscattered signal. These two strategies improve the distance of down-link and up-link significantly at the same time.

A. Antenna Design for Increasing the RSS

To boost the RSS over a long distance, we develop unique designs of high-gain antennas for the reader and tag.

To be able to apply for autonomous driving, the following requirements for antennas must be met: 1) *high-gain directional*—the angle between reader and tag is tiny since the road width is much smaller than the communication distance. According to calculations, assuming the communication distance is 50 m (road conditions are recognizable by drivers and cameras) and the road width is 15 m, the angle between the direction of vehicle speed and the tag is approximately 16.7°. As the angle decreases with distance, we can narrow down the sensing region and concentrate the energy in the beam range of 30° to improve the gain of antennas; 2) *large bandwidth*—in order to reduce repeated design and cost, we hope that the antenna will work well in all UHF RFID frequency bands (840–956 MHz), allowing us to expand our work in the future; and 3) *deployability*—antennas should be conformal to autonomous vehicles and road infrastructures.

It is efficacious to utilize a directional antenna to concentrate the beam to maximize antenna gains. However, the beam width of a commercial single horn directional antenna or Yagi antenna is insufficient, resulting in energy waste and interference between several devices. In spite of the fact that antenna arrays made of these antennas will spatially concentrate radiation energy on the dominant path and prevent interference from undesirable paths, they will be too bulky to be deployed.

Inspired by the microstrip antenna, we print the array antennas on the dielectric substrate as conformal antennas suited for vehicles and infrastructures. We design the reader and tag separately since they work in different modes and will be deployed on different objects (the reader antenna is frequently installed horizontally on the top of a car, as far away from the ground as possible, whereas the tag must be integrated into road signs or traffic lights which are perpendicular to the ground). To avoid polarization mismatch loss, they should have the same polarization mode.

1) Microstrip Array Antenna for Tag (Analysis of the Tag Antenna): The scattered field of an antenna is generally divided into two parts: structural scattering item and antenna-mode scattering item. It can be stated as follows:

$$\vec{E}^{s}(Z_l) = \vec{E}^{\mathrm{st}}(Z_c) + \vec{E}^{\mathrm{an}}(Z_l). \tag{3}$$

$\vec{E}^{\mathrm{st}}(Z_c)$ is the structural term that refers to the scattering of electromagnetic waves when the antenna is treated as a scatterer, and the impedance is perfectly matched to the load. It relates to the external physical parameters, such as material and size. $\vec{E}^{\mathrm{an}}(Z_l)$ is the antenna-mode term that refers to the secondary radiation induced by the mismatch with the load when electromagnetic waves irradiate the antenna. It is directly related to the antenna's radiation performance and the antenna impedance's matching state, which is similar to the active radiator. The antenna of the backscatter tag is a mixture of scattered and secondary radiation since we modulate carrier signals by switching the impedance of the antenna load. As a result, the strength of the backscattered signal is determined by both items.

Antenna Array Design: To satisfy the requirement 1), we try to ameliorate the structural scattering term by enlarging the surface area. Microstrip planar antenna is an excellent choice

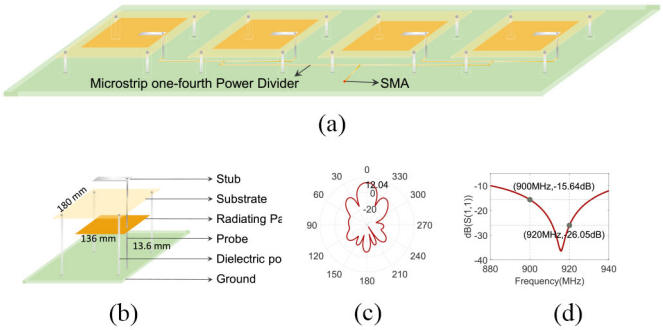

Fig. 4. HFSS simulation of Tag antenna. (a) Microstrip array antenna for Tag. (b) One radiation unit. (c) Radiation pattern. (d) S11 parameter.

since they radiate the most energy in front of the patch, which accords with the deployment requirement 3) of the tag. An array made up of several microstrip planar antenna elements can be designed to obtain higher gain with a specific direction, as shown in Fig. 4(a). Every radiation patch is a rectangle.

The number and spacing of array elements affect antenna gain and direction. On the one hand, the beamwidth narrows as the number of antenna elements increases, which causes the array to become larger. Given the size constraint, we first set the element number as 4 to verify the feasibility of the array antenna. Then, we design a parallel feed power splitter to divide the input power into four channels. It is simple to obtain the desired amplitude and phase by modifying the power divider ratio and adjusting the microstrip line size. Each transmission path of the power splitter from the feed SMA to each element has the same length in our design.

On the other hand, a large sidelobe is caused by a large interval, while a tiny interval causes coupling between antenna elements. We simulated element spacing of 200 mm ($0.5\lambda - \lambda$) to attain a good beamforming performance, which may be optimized using optimization algorithms. The total length is 800 mm, and the width is 300 mm.

Broadband Microstrip Antenna With Minimal Loss: The bandwidth BW of the antenna is inversely proportional to the quality factor Q value. To meet the requirement 2), we need to decrease Q. Vandensande *et al.* [38] gave the expression of Q as follows:

$$Q_r = \frac{C\sqrt{\varepsilon_e}}{4f_r h}$$

where ε_e and h are the dielectric constant and thickness of the substrate, respectively, and f_r is the center frequency. The dielectric constant and substrate thicknesses are h and ε_e, respectively, and fr is the center frequency. Thickening the dielectric substrate is the simplest method for lowering Q. However, it lowers radiation efficiency. Therefore, figuring out how to minimize the loss while maintaining the required bandwidth is challenging. Selecting F4B with a low dielectric constant and low dielectric loss (0.003) can also reduce the Q value. However, its price is high, about six times that of FR4, with a slightly higher dielectric constant and transmission loss (0.02). We decided to use FR4 as the substrate considering the tradeoff that tags would be used on the road in huge numbers and that prices should be kept as low as feasible.

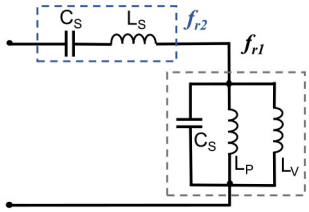

Fig. 5. Equivalent circuit of L-probe-fed microstrip antenna.

To provide a sufficient bandwidth with minimal transmission loss using the low-cost substrate material FR4, we adopt the L-shaped feeding mechanism to increase the bandwidth [39], [40], [41]. As shown in Fig. 4(b), L-shaped probes feed the radiation patch by coupling. This design compensates for part of the loss caused by FR4 since its dielectric layer is an air layer with free and lowest dielectric constant (= 1). We can equate one element of the array antenna to an RLC circuit, as shown in Fig. 5. The original rectangular microstrip patch antenna can be equivalent to an LC parallel resonant circuit. When L-probe is added, a nonnegligible reactance is generated. They produce a resonant frequency of f_{r1}. In addition, the vertical probe across the upper suspended dielectric substrate generates inductive reactance L_P, and the horizontal stub generates capacitive reactance C_S with the patch, respectively. They combine to create a series resonant circuit with a frequency f_{r2}. The reactance of the series and parallel resonant circuits tends to be offset near the resonant frequency, which prevents the abrupt decline in reactance when deviating from the resonant frequency and broadens the frequency band.

The inductance L and capacitance C in Fig. 5 are related to the length of the probe h and the size of stub and patch $W \times H$, which can be expressed as follows:

$$L = F_1(f_r, h, W, H), C = F_2(f_r, h, W, H). \quad (4)$$

We can provide the required resonant frequency and bandwidth by adjusting these parameters. The spacing between the horizontal stub and the patch is limited by commercially determined dielectric substrate thickness (1.6 mm for FR4). According to the empirical formulas given by [42], we calculate the initial values of the width and length of the radiation patch and stub. Finally, the optimum values are determined using the high-frequency structure simulator for strict numerical simulation. In our simulation model, the radiation patch is 136 mm × 136 mm, the suspend substrate is 180 mm × 180 mm, the vertical probe is 13.6 mm, and the horizontal microstrip stub is 5 mm × 9 mm. In addition, we can change the antenna's polarization by altering the stub's direction.

2) Microstrip Yagi Array Antenna for Reader: Reader antennas are generally mounted on the roof of vehicles. To minimize the disruption to the aerodynamics of vehicles, we try to flatten the antenna as much as possible. We naturally try to make an end-on-fire antenna by printing the Yagi array on the dielectric substrate to meet all the above requirements.

As illustrated in Fig. 6(a), components of this Yagi microstrip antenna array are arranged in parallel on a plane,

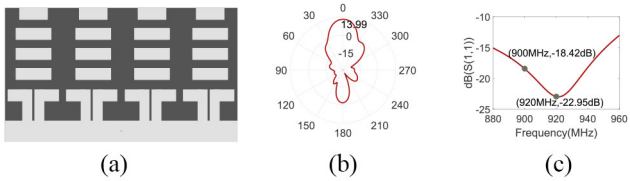

Fig. 6. Microstrip Yagi antenna array design for reader. (a) Top layer. (b) Radiation pattern. (c) S11 parameter.

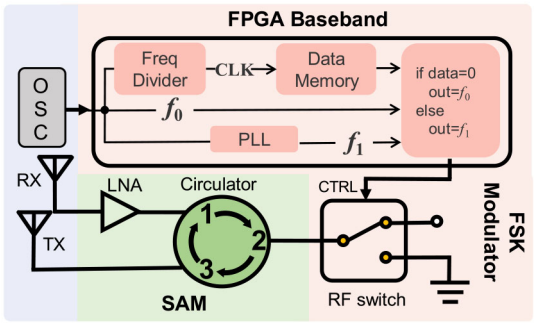

Fig. 7. Hardware Design of tag.

making it a plane antenna that conforms to the shape of vehicles. Every Yagi antenna consists of a driven element, a reflector, and several directors [43]. The reflector ensures the antenna's one-way radiation and directors increase its directivity. They are electromagnetically coupled to each other. A four-channel microstrip power splitter is also employed, similar to the tag antenna design. It enhances bandwidth through coupling feeds as well. To reduce transmission loss within an acceptable price range, we choose F4B as the dielectric substrates with the thickness and relative permittivity of 1.5 mm and 2.65 since the cost of the vehicle itself is relatively high and the cost of an antenna can be appropriately high to reduce loss. Our simulated array measures 700 mm in length and 430.28 mm in width. The spacing of the array elements is 123 mm. The reflector is 700 mm × 80 mm. The size of the four directors is 120 mm × 30 mm, 110 mm × 30 mm, 110 mm × 30 mm, and 90 mm × 35 mm.

Simulation radiation patterns of the two antennas are shown in Figs. 4(c) and 6(b), respectively, indicating that the antennas of the reader and tag can concentrate most of the energy within 23° and 21° and the gain can reach 14 and 12 dBi.

S_{11} results measured by the network analyzer are shown in Figs. 4(d) and 6(c), respectively. S_{11} of the tag antenna at 900 and 920 MHz is −15.64 and −26.05 dB, which illustrates that 95% of the power will be transmitted and 80% be received at least theoretically, which meets our design requirement. Similarly, for the reader antenna, 88% ($S_{11} = -18.42$ dB) of the power will be transmitted and 93% ($S_{11} = -23.4$ dB) be received at least theoretically.

B. Tag Design

To increase RSS further, we present the circuit design of the tag through FSK implementation, SAM, and semi-synchronous structure as shown in Fig. 7.

1) FSK Modulation Implementation: The FPGA receives the clock signal supplied by the oscillator and then separates it into three pathways. The first path is directly connected to the modulation module to produce the frequency f_0 for bit "0," the second path is connected to the phase lock loop (PLL) to generate f_1 for bit "1," and the third path is connected to a frequency divider to generate a clock signal for desired bit rate. If transmitted data is bit "1," the FPGA outputs a square signal with the frequency of f_1. On the contrary, the frequency of the output square signal is f_0.

The output signal of FPGA controls the RF switch to toggle between two impedance to modulate the incident signal [44], which essentially is analogous to a mixer. Finally, when the carrier signal reaches the tag, the backscattered signal can be represented as follows:

$$\mathrm{BS}(t) = \begin{cases} \cos(2\pi(f_{c1} + \Delta f \pm nf_0))t, & \text{data} = 0 \\ \cos(2\pi(f_{c1} + \Delta f \pm nf_1))t, & \text{data} = 1 \end{cases}$$

where $n = 1, 3, 5, \ldots,$ odd, f_{c1} is the frequency of the incident carrier, and Δf is the frequency shift between incident and backscattered signal. Signals above the second harmonic can be ignored because of their very low amplitude. Low frequency signals $\cos(2\pi(f_{c1} - nf_0)t)$ and $\cos(2\pi(f_{c1} - nf_1)t)$ are filtered out at the receiver.

2) Signal Amplification Module Design: Long-distance transmission causes a weak signal to reach the tag. However, if the income signal or reflected signal can be enhanced, the reader's RSS can significantly improve. As a result, we are considering if we can add an amplifier to the tag's RF front-end to boost the power of incident or backscattered signals to push the communication range.

Unlike the active radio architecture with separate sending and receiving links, the tag only has one antenna since it modulates data by toggling the load impedance of the antenna. However, the amplifier is unidirectional. When it is connected positively to the modulating antenna port, the incoming signal is amplified while the reflected signal is blocked. If we connect the amplifier reversely to the port, most energy of the incoming signal will be blocked by the amplifier. The backscattered signal from the tag is not necessarily amplified or even reduced. Thus, designing the amplification module with one antenna port is a challenge.

A straightforward solution is splitting the link in half using a power splitter or an RF tee connector. However, since the amplifier is unidirectional and only a portion of the energy may be input or backscattered, which causes part of useful energy to be wasted, as testified in Section VII-B.

Inspired by the circulator, which is commonly used in full-duplex radio [45], we can use its property to isolate the incident and backscattered signals of the tag.

Specifically, as shown in Fig. 7, circulator is a three-port unidirectional transmission device. We connect two antennas to the port (1) and port (3) of the circulator and connect the tag to the port (2). The carrier signal passes through port (1) to port (2). Most of the energy will be reflected by port (2) due to impedance mismatch and flow to port (3). Note that only a tiny part of the signal power will be returned to port (1)

since a commercial off-the-shelf (COTS) circulator can provide isolation of 25 dB between the two ports, which has a slight influence on the backscattered signal.

After separating the ULink and DLink via circulator, we can add an amplifier to amplify the incident signal or reflected signal. From the cascade circuit noise figure

$$F = F_1 + \frac{F_2 - 1}{G_1} + \frac{F_3 - 1}{G_1 G_2} + \cdots$$

G_n is the gain of the N_{th} element in the receiving chain. It can be known that the noise figure of the first stage amplifier (F1) plays a dominant role, while that of the subsequent stage has less influence. Thus, to decrease power consumption and minimize the noise figure of the entire tag circuit, we connect an LNA to port (1) to improve the SNR of the signal arrived at the tag. In some scenarios where sufficient power is supplied, another PA can be added to achieve a longer distance. Note that we are just here to demonstrate the feasibility of our amplifier module design. The circuit of LNA can be further optimized by utilizing a lower-power chip to cut power consumption drastically in the future.

3) Semi-Synchronous Structure Design: To increase the DLink range, we adopt a semi-synchronous structure, which makes the tag free of activation energy and minimizes the modulation delay. Specifically, our tag does not have a detection circuit, and we locate the synchronous operation to the high-sensitivity receiver. To demodulate transmitted data correctly, the tag must broadcast a known synchronous sequence (SS) before data to indicate when it begins to modulate. The reader correlates the local time-domain signal $P(t)$ generated by the SS sequence with the received baseband signal $y(t)$. Since the ADC discretely samples the signal, the correlation distribution can be represented as follows:

$$R(m) = \sum_{t=-\infty}^{\infty} P^*[t] y[t+m]$$

where m denotes the sliding stride. Each peak in the correlation distribution represents the package's starting point. To have a higher detection accuracy of the start sample under low SNR, the sequence must have good correlation properties, such as the pseudo-noise code sequence (PN). There is a tradeoff in SS selection: the longer the SS, the more precise the start sample detection is, but it also means less data is delivered every second.

In summary, when this mode is adopted, the tag is always in an operating mode, no matter whether there is a carrier signal. SS needs to be added before valid data. The receiver receives the backscattered signal and correlates it with the known SS sequence signal. After finding the start point of the packet, the valuable data are demodulated and decoded. This semi-synchronous method takes advantage of the high sensitivity of the receiver to eliminate the need for low sensitivity detection of low power tags, resulting in a considerable increase in Dlink distance. Although this mode will lead to a waste of tag energy when there is no vehicle, we believe that the increased detection distance justifies the energy sacrifice since the power consumption of the tag itself is smaller than that of the active transceiver.

VI. Reduce BER to Improve Communication Range

In this section, we improve communication range by reducing BER at a low SNR through two measures. First, unlike traditional FSK demodulators with independent processing models of denoising and demodulation, we propose a DL-based FSK demodulator EC-Net that jointly optimizes the two models to reduce demodulation BER significantly. Second, to combat the influence of noise and interference to improve communication robustness, we adopt convolutional codes for the transmitted data of tag. Meanwhile, instead of using the classification results of EC-Net directly for decoding and error correction, we design a soft decoder whose input is special quantized values of probabilities output by EC-Net. The design of the EC-Net demodulator (Section VI-A) and encoder-decoder (Section VI-B) is then detailed.

A. Design of Deep Learning-Based EC-Net Demodulator

Various undesirable factors typically influence wireless channel transmission. The backscattered signal arriving at the reader can be simplified as follows:

$$r(t) = h(t) * BS(t) e^{j\phi t} + n(t) + i(t) \tag{5}$$

where perfect channel pulse response $h(t)$ and phase offset induced by hardware imperfections ϕ are difficult to estimate in practice. $n(t)$ and $i(t)$ are noise and interference.

Conventional receivers generally recover the transmission data from a noisy channel by performing a series of complicated operations, including carrier synchronization, symbol synchronization, channel estimation, and equalization, which are challenging to implement in real-world situations. Contrarily, incoherent FSK demodulation (FSK-CD) is frequently applied in practice since it can be implemented quickly without needing phase information. Unfortunately, demodulating with a denoised signal, FSK-CD may produce a higher BER since it uses amplitude information converted from frequency information for decision. Whereas popular denoising techniques (such as wavelet denoising and the threshold method) can reduce noise, they also damage valuable signals.

To this end, we propose an end-to-end framework EC-Net that extends the signal enhancement to incorporate the high-level goal of demodulation. As shown in Fig. 8, the network consists of an enhancement network (EnhancerNet) and a classification network (ClassifierNet), corresponding to denoising and demodulation models of FSK-CD separately. Input to the network is polluted-clean signal pairs and class labels for training, and the output value denotes the score that the input belongs to each category. In this architecture, EnhancerNet is trained to obtain "enhanced" signal features as the input of ClassifierNet. Then, ClassifierNet trains these "enhanced" features and true labels to predict the class of the current input signal feature.

There are two reasons for making EC-Net more suitable for demodulation. First, DL has certain advantages for feature extraction when the wireless channel is disturbed by noise and interference. Second, unlike traditional signal processing, where denoising is only loosely related to the classification performance, the explicit goal of EC-Net is to maximize

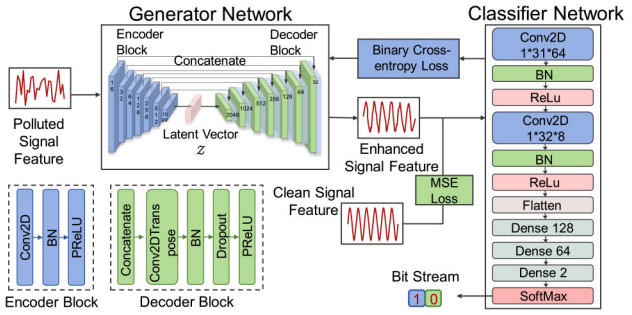

Fig. 8. Overall architecture of EC-Net.

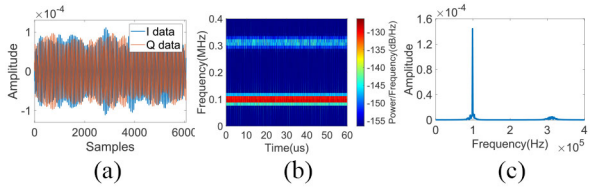

Fig. 9. Features of bit "0." (a) IQ data. (b) Time-Freq. (c) Amp-Freq.

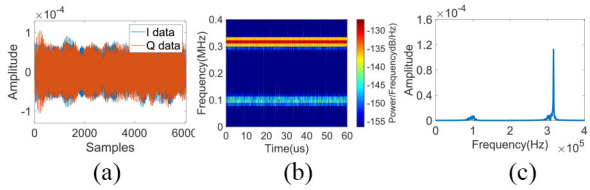

Fig. 10. Features of bit "1." (a) IQ data. (b) Time-Freq. (c) Amp-Freq.

the probability of ClassifierNet making the right decision mainly. In other words, EC-Net selectively enhances only those informative features that lead to better classification accuracy.

Regarding the delay, although the demodulation model training requires a long time to find the optimal parameters, testing can be done in a very short time since test data need to run only once using the trained model parameters.

1) Design of EC-Net Demodulator: Following that, we present the specific design of two key components and our end-to-end architecture.

EnhancerNet: We train the enhancer network to regenerate "enhanced" features of "polluted" signals with "clean" signals as ground truth. Here, the "polluted" and "clean" signals have low SNR and high SNR in the actual scene with noise, respectively. Its inputs are "polluted" signal features $X(f)$ together with the latent variable z, and its output is the enhanced feature $R(f) = E(X(f))$.

The structure of EnhancerNet is similar to that of Encoder-Decoder [46] which is a fully convolutional network. Respectively, EncoderBlocks extracts and transforms valuable information in the input feature into a low-dimensional vector by convolution, while DecoderBlocks is to regain original dimension features by operating transposed convolution.

ClassifierNet: We transform signal demodulation into a typical binary classification problem. The ClassifierNet aims to classify the input signal feature as bit "0" or "1." It consists of convolution, batch normalization, activation, and dense layers. The first three layers are for feature extraction. The dense layer is to realize the function of the classifier by mapping the learned "distributed feature representation" into the label space.

End-to-End EC-Net: A simple network is to feed samples into an EnhancerNet to get enhanced signal features and then feed them into a ClassifierNet for classification, which we call GDC-Net. In this way, classification and enhancement are completely independent parts and are processed separately. The process of feature enhancement is not affected by the classification results.

However, as previously mentioned, our ultimate aim is to improve classification accuracy rather than make the enhanced feature precisely approximate the clean signal. Thus, we propose EC-Net, which propagates the classification objective back to the enhancement step by utilizing an iterative feedback loop to selectively extract informative features from enhancement techniques to improve classification accuracy further.

We fine-tune the whole pipeline until convergence. The joint optimization allows the loss gradients from the ClassifierNet to also back-propagate through the EnhancerNet, optimizing the enhancement parameters for classification. The total loss function is based on calculating the mean squared error (MSE) between the ground truth signal $T(f)$ and the network's predicted output $G(X(f))$, as well as classification loss, which can be expressed as follows:

$$E_{\text{Loss}} = \text{MSE}(T(f), G(X(f))) + \left[-\left(y \log\left(P_{G(X(f)}\right) + (1-y)\log\left(1 - P_{G(X(f))}\right)\right)\right] \tag{6}$$

where y is the true label "1," $P_{G(X(f))}$ is the predicted probability of classifying as "1" after the output layer with softmax as the activation function. This architecture enables joint optimization by end-to-end propagation of gradients in ClassifierNet and EnhancerNet with a stochastic gradient descent (SGD) optimizer.

2) Feature Design Choices: As we all know, different features have different impacts on classification accuracy. Below are some currently accessible signal features visualized in Figs. 9 and 10, followed by an analysis of how we should choose.

IQ Data in the Time Domain (IQ): The continuous samples of the bit "0" and "1" in the time domain are shown in Figs. 9(a) and 10(a). The time-domain feature is obtained directly from the receiver through the I and Q channels, i.e., the received signal is multiplied by $\cos(2\pi f_{c2} t)$ and $\sin(2\pi f_{c2} t)$, respectively, and then combined them to get discrete complex samples. f_{c2} is the carrier frequency after frequency shifted. We put the I channel samples into the first row and the Q channel samples into the second row to form a $2 \times n$ (n = sampling rate/bit rate) matrix as a training sample.

Time-Frequency (TF) Features: TF images obtained by short time Fourier transform (STFT) are shown in Figs. 9(b) and 10(b). However, these images have many redundant data,

increasing computational complexity, and memory consumption. In order to reduce the size of one sample, we only choose the data of around f_0 and f_1 with several rows, respectively, in the power spectral density matrix to form a 400×22 matrix as a sample.

Amplitude-Frequency (FFT) Features: To get the amplitude-frequency features, we carry out the fast Fourier transform (FFT) on the signal of bit "0" and "1" after the bandpass filter, which are visualized in Figs. 9(c) and 10(c).

The sample size and information content are the two factors we consider while selecting features. On the one hand, since the tag uses FSK modulation, the TF and FFT features can better characterize the difference between bit "0" and "1" bits. However, after FFT, useful information about the original signal may be lost. On the other hand, unprocessed temporal IQ signals can achieve higher classification results by exploiting convolutional networks' excellent feature extraction ability. However, compared with the FFT features, the sample size of the IQ feature under the low bit rate is relatively large. Which feature is chosen depends mainly on the deployed scenario. The FFT feature can minimize the size of one sample to reduce training and testing time for low bit rates; for high bit rates, we can utilize the IQ feature without FFT preprocessing to reduce latency. We show test results of these three features in Section VII-B.

B. Channel Encoding and Soft-Decoding

To further reduce BER and improve robustness in the real wireless channel with noise and interference, we adopt channel coding to correct transmission errors and resist random noise, which essentially adds redundancy to transmitted data. The convolutional encoding provides excellent error-correcting ability since the encoded output bits are related to both the current bit and the previous. Additionally, the implementation of a convolutional encoder is very simple and suitable for low-power tags.

1) Convolutional Encoding for Tag: We can use (n, k, m) to describe the convolution code, indicating that the convolution code can encode k bits into n bits for output. The encoding constraint length is m, and the bit rate is defined as k/n. We can express the polynomial generator matrix of the convolution encoder as follows:

$$G(x) = \left[g_1(x), \ldots, g_n(x)\right] \tag{7}$$

where g_i is the generator polynomial of the ith output

$$g_i(x) = a_{i,0}x^0 + a_{i,1}x^1 + \cdots a_{i,m-1}x^{m-1} \tag{8}$$

where $a_{i,j}$ is the coefficient (0 or 1) on the jth term of $g_i(x)$.

There is a tradeoff we need to balance is that a lower coding rate consumes more FPGA resources but provides better error correction. Based on the results of our tests for different coding rates in Section VII-B2, we choose a 1/3 convolutional encoder for our tag implementation, which only requires three registers and three XOR gates.

2) Soft Decoder: Viterbi is a standard convolutional code decoding approach that utilizes dynamic programming to seek the maximum probability output to correct errors made during signal transmission and demodulation. The most straightforward approach is to input the EC-Net's classification result "0/1" sequence into the Viterbi decoder. However, statistical characteristics of channel faults in the received signal will be missed.

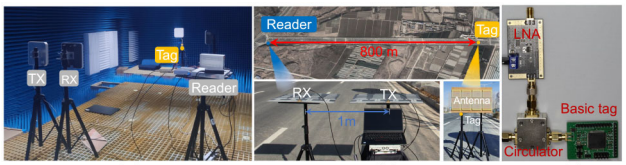

(a) (b) (c)

Fig. 11. Experimental deployment. (a) Anechoic chamber. (b) Outdoor road. (c) Tag prototype.

To improve error-correcting ability, we design a soft decoder combined with EC-Net, which takes advantage of probability information. Specifically, the first step is to attain the probability using EC-Net, and we quantify the probability to an integer from 0 to $2^m - 1$. Here, m is an integer greater than 0. It is worth noting that the quantization method and granularity will affect the final decoding performance. The larger this value means, the finer the granularity we quantified, which does not necessarily lead to better decoding performance. According to our simulation test, we set m to 3 here. That is, the quantified values are from 0 to 7 ($2^3 - 1$). Then, we utilize these values as the input of Viterbi, whose specific algorithm is described in [47].

VII. Evaluation

We deploy our system in two environments: 1) an anechoic chamber as shown in Fig. 11(a), with little interference from other wireless signals and 2) beside the road as shown in Fig. 11(b) where there is a small amount of traffic and pedestrians to avoid security issues.

We start with microbenchmark experiments conducted in the anechoic chamber to verify the feasibility of the tag design and EC-Net demodulator with the soft decoder in improving range. Following that, we assess the whole system's performance and conduct a moving case study in which a vehicle equipped with a reader identifies a roadside backscatter tag.

These experimental deployments and parameters are different, which will be listed in the corresponding experiment later. One thing that should be noted is that all data processing is done offline after the data collection.

Evaluation Metrics: To obtain stable evaluation results, the total number of samples of bit "1" and bit "0" we obtained at each distance (or attenuation value) is approximately 10^5 for each experiment. We use BER to assess the system performance, defined as the number of bits decoded in error divided by the total number of transmitted bits.

A. Implementation

Reader Implementation: The reader of AllSpark is implemented on the software-defined radio (SDR) NI USRP-2954R with a laptop for processing baseband signal. The USRP uses array antennas we designed. The baseband signal is a 100-kHz

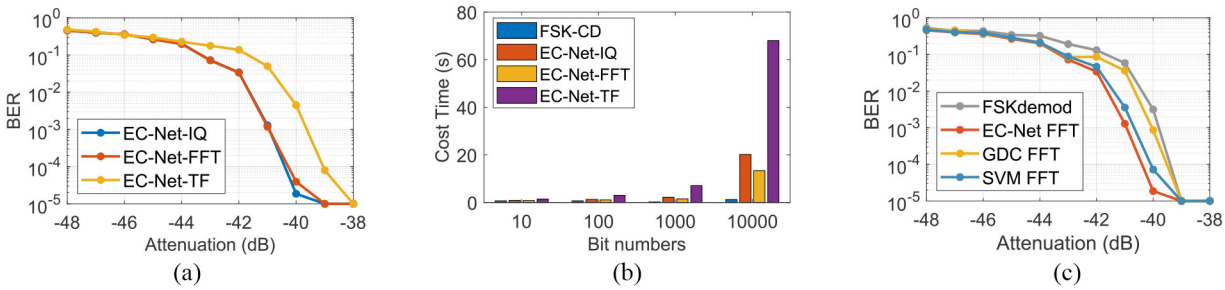

Fig. 12. Verification of EC-Net. (a) Demodulation BER of EC-Net with different features input; (b) Demodulation time required for different features as the total number of bits increases; (c) Demodulation BER of different methods as attenuation value increases.

cosine wave, and the TX carrier frequency and RX frequency are 900 and 920 MHz, respectively. We set the sample rate of the reader as 6 MHz by default. Furthermore, we use an RF power amplifier to increase the transmission power to 33 dBm. Our decoding algorithm is implemented on the offline software platform, which may be extended to USRP in future work.

Tag Prototype: As shown in Fig. 11(c), the tag is prototyped using an amplifier [48], a coaxial circulator [49], and the basic tag. The basic tag is a four-layer printed circuit board (PCB) with standard electronic components. As HitchHike [44] recommended, we choose the low-power Microsemi IGLOO Nano AGLN250-v100 as FPGA [50] and ADG902 [51] as RF switch. The steady clock for the FPGA is provided by a 20-MHz oscillator ASTX-H11 [52].

B. Micro-Benchmarks

The tag is stuck to a tripod 4.5-m away from the reader. For a fair comparison, we symmetrically add adjustable attenuators at the transmitter and receiver to simulate path loss of ULink and DLink. Since DLink and ULink have the same distance, we set the two attenuators to the same value for each trial.

1) Feasibility Verification of EC-Net Demodulator: We first evaluate the performance of the EC-Net demodulator. We compare the BER of different features (given in Section VI-A2) and different demodulation methods under the same attenuation value.

Data Collection in the Real World: The simulation data with the Gaussian noise cannot represent the signal of a certain distance in the actual situation. Thus, we train the EC-Net with actual data collected by USRP. To acquire "clean" data as labels for "polluted" data measured in various ranges, we use the other RX channel without attenuation and place its antenna near the tag. Under different communication distances, we split all samples into the training set, validation set, and test set according to 5:1:4 for training and testing of EC-Net.

Different Features Comparison: We compare the performance of three features using the EC-Net demodulator. Each bit is treated as an input sample. Each IQ sample is a 2×6000 matrix, whereas the FFT sample is a 1×2048 matrix intercepted between 100 and 320 kHz. Similarly, the TF feature is a 400×22 matrix, the intercept of the power matrix processed by STFT. Training will be costly and challenging if the frequency resolution of TF features is guaranteed to be the same as that of FFT. Thus, we balance sample size and frequency resolution to choose more optimal FFT points.

Fig. 12(a) shows the result, with the x-coordinate indicating the attenuator value and the y-coordinate displaying the demodulation BER. We can observe that the FFT and IQ features have a similar BER of below 10^{-2} when attenuation is less than -41 dB, while the TF feature has the lowest performance since the STFT processing causes more information loss.

Better demodulation results are achieved with higher FFT resolution, but it also takes longer. Fig. 12(b) indicates that FSK-CD is superior to EC-NET demodulator in terms of processing time. Compared with FSK-CD, although EC-Net+FFT cost an extra 1.3 s for demodulating 1000 bits, the processing delay is 43.25-m under high-speed 120 km/h, which can still meet the security requirements under the detection distance of 600 m. In addition, IQ and FFT feature shows a considerable advantage over TF, whether ten samples or 10 000 samples. Considering data processing time and demodulation performance, the FFT feature is used in our evaluation by default.

Different Methods Comparison: The comparison result of EC-Net, SVM, GDC-Net, and FSK-CD (contains bandpassing, multiplier, low pass filtering, and sampling decision) is shown in Fig. 12(c). We can see that EC-Net performs better than others. SVM also has a lower BER since it iterates times to search for the optimal parameters, leading to a long demodulation time. We notice that the EC-Net demodulator does not improve over the FSK demodulator when the attenuation value is larger than -45 dB since the SNR is too low.

Effect of Bit Rate on EC-Net Demodulator: Then, we evaluate demodulation performance under bit rates of 1, 2, and 3 kb/s. The deployment is identical to the one described in the previous section. We change tags with the same sent data but different bit rates at each attenuation setting. As shown in Fig. 13(a), we can observe that BER can achieve 10^{-5} at 1 kb/s when both attenuators are set to -39 dB, while attenuation values from -39 to -45 dB. The BER slightly decreases with the bit rate increase since a sample under a higher bit rate will contain fewer sampling points. Regarding DL, fewer sample information leads to lower classification accuracy.

2) Effectiveness of Convolutional Encoding and Decoding: We use the basic tag without the SAM to test the efficiency of convolutional encoding and soft decoding in decreasing BER.

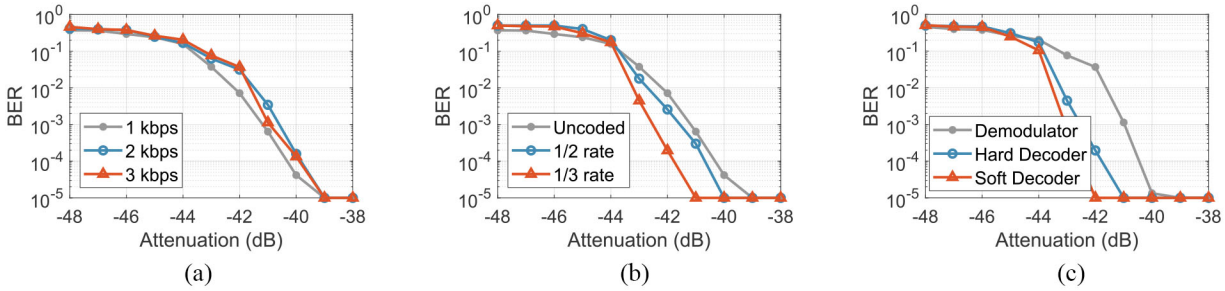

Fig. 13. Results of coding and decoding. As attenuation value increases, BER versus (a) tag modulates at different bit rates 1, 2, and 3 kb/s; (b) tag adopts different convolutional coding rates of 1/2 and 1/3; (c) after EC-Net demodulator, reader use hard decoder and soft decoder, respectively.

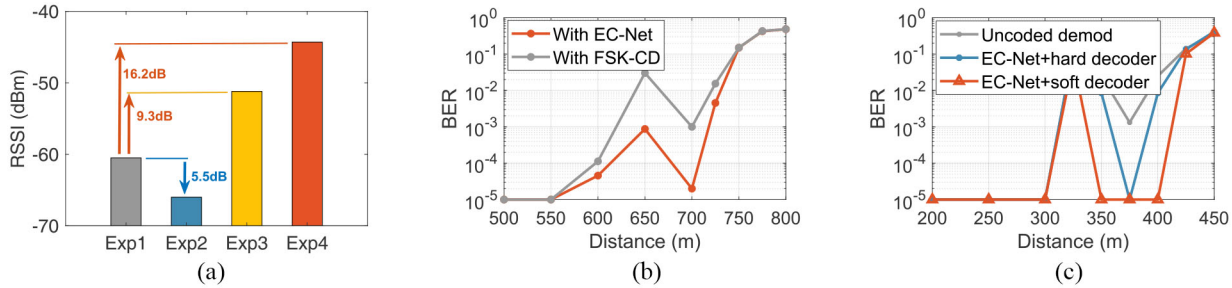

Fig. 14. (a) EXP1-EXP4 represents four deployments: basic tag, tag with a single amplifier, tag with an amplifier and an RF tee connector, and tag with SAM, (b) is the overall performance of AllSpark, (c) performance without SAM.

We employ the EC-Net demodulator to demodulate first by default.

Different Coding Rates: We test three prototypes with various data encoding rates of 1/2, 1/3, and noncoding to see how much gain convolutional encoding can provide.

The transmitted data of the tag is a randomly generated 96-bit sequence. For nonencoded data transmission, the data rate we set as 1 kb/s. To ensure that the same amount of information bits are transmitted each second, we set the bit rate of the tags with $1/2$ and $1/3$ code rates to 2 and 3 kb/s, respectively. The comparison result is shown in Fig. 13(b). The horizontal axis is the values of each attenuator, and the vertical axis is the BER of the demodulator (for uncoded tag) or decoder (for encoded tags). Compared with uncoded tags, both $1/3$ and $1/2$ convolutional encoding rates with Viterbi decoding provide significant coding gains. When the attenuator value is set to -41 dB, the BER of $1/3$ code rate can achieve 10^{-5}, which meets the requirement of reliable communication, while $1/2$ code rate has a slightly worse BER of 10^{-3}.

Hard and Soft Decoding Gain: In order to prove the gain of the soft demodulator we proposed, we perform EC-Net demodulation for the unencoded tag and perform hard and soft decoding for 1/3 code rate tag after EC-Net demodulation. The result in Fig. 13(c) shows that the soft decoder has 2 and 6 dB gains compared with the hard decoder and uncoded demodulator.

3) Feasibility Verification of RF Front-End: To verify the advantage of the specially designed tag, we compare three assembled prototypes with a basic tag. We use an Agilent Technologies hand-held spectrometer as the receiver to measure RSS. EXP1-EXP4 represents four prototypes: 1) basic tag; 2) tag with a single amplifier; 3) tag with an amplifier and an RF tee connector; and 4) tag with SAM. The results in Fig. 14(a) show that the SAM we proposed for the tag has the highest gain compared with the basic tag.

The reflected signal will be blocked since the amplifier is unidirectional, which causes EXP2 to have a loss of 5.5 dB. EXP3 amplifies half of its power even though it separates the transceiver links.

4) Power Consumption: Simulation results of FPGA in the Libero platform show that the static power consumption is 38.1 μW, the dynamic power consumption is 2965.887 μW, and the total power consumption is 3003.987 μW. According to the calculation of the parameters in datasheets, the RF switch ADG902 consumes only 0.3–3 μW. The oscillator ASTX-H11 consumes up to 14.4 mW to generate a 20-MHz clock. The LNA we used consumes 180 mW, which can be reduced by designing the circuit specially and using amplifier chips with lower power consumption. For the actual power consumption measurements, we use HV Power Monitor [53] to supply a constant 3 V to enable the tag and measure the power consumption. The total nominal and actual maximal power consumption of the tag is 197.407 and 244.2 mW, far less than the energy needed for an active transceiver such as RSU [54] in DSRC. Although our current tag needs an external power supply to provide energy, it is possible to provide energy through high-power solar panels and RF energy by implementing our tag on IC in the future.

C. Practical Communication Performance

This section evaluates the BER performance at various distances and investigates the maximum backscatter range. Finally, we respond to the topic of whether AllSpark can be used in a moving scenario. Based on the above analysis and

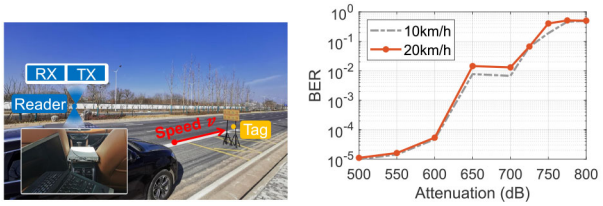

(a) (b)

Fig. 15. Mobile scenario and decoding performance. (a) Mobile experimental deployment. (b) Impact of the moving speeds.

benchmark experimental results, we use the tag with SAM and 1/3 code rate as the target tag and utilize the EC-Net demodulator and soft decoder across all experiments.

In addition, we choose a 15-bits m-sequence as the SS due to its good auto-correlation and cross-correlation.

In these experiments, we keep the reader fixed and move the tripod with the tag to various positions between 100 and 800 m. We calculate the BER at the reader as a function of the distance between reader and tag. Fig. 14(b) shows the result. We can see that the reliable transmission (BER less than 10^{-4}) is possible at 700 m, which meets our long-range requirement. We observe slightly anomalous results at 650 m, possibly due to other strong signal interference when we collected data at this distance. By contrast, if we adopt FSK-CD, although it can achieve 700 m, the BER is slightly greater than 10^{-3}, and BER is sharp when there is strong interference at 650 m. This result shows that EC-Net has lower BER and more stable communication over the same distance, which has the same conclusion as Fig. 12(c).

In addition, as shown in Fig. 14(c), we test the maximum distance of AllSpark without SAM. Even though the tag does not have the amplification module, the system can attain a relatively stable transmission range of 400 m (BER $\leq 10^{-4}$). The result means SAM has a range improvement of 300 m. Also, comparing the blue and red lines shows that the soft decoder is superior to the hard decoder at 350 and 400 m. The comparison between the red line and the gray line indicates that the BER of using channel coding and our proposed soft decoder is reduced by two orders of magnitude compared without channel coding, proving that our EC-Net demodulator and soft decoder can make the system have better robustness.

D. Mobile Application

Finally, we evaluate the performance of AllSpark in mobile scenarios where the tag is placed at a fixed location, and the reader is mounted in a car that moves at different speeds of 10 and 20 km/h. At every speed, we perform 20 experiments and transmit at least 960 bits (i.e., ten packets) every time in total. Snapshots of the setup are shown in Fig. 15(a).

The results in Fig. 15(b) indicate that the decoding BER slightly increases at a higher speed compared with a lower speed. Even at 600 m, BER does not exceed 10^{-4} at the speed of 20 km/h since that although high speeds lead to doppler shift, it has little effect on the frequency characteristic of the received baseband signal and EC-Net demodulation. Therefore, AllSpark has the potential to be used for autonomous driving.

VIII. Conclusion

We present and implement a long-range backscatter communication system AllSpark. It significantly improves distance through a combination of hardware and software solutions. On the one hand, we specially design a tag with an amplification module and high gain microstrip array antennas for the tag and reader to improve RSS. On the other hand, DL-based EC-Net demodulator and soft decoder are implemented at the reader to withstand burst interference to minimize BER under low SNR, which can be extended to applications requiring decoding at low SNR. The preliminary results show that with the data rate of 1 kb/s, AllSpark can provide a reliable communication range of 700 m. Even if the vehicle equipped with the reader is moving, it also could achieve a communication range of 600 m, which is adequate for real-world driving scenarios. The architecture of AllSpark also may be expanded to enable a wide range of applications, for example, counting thousands of products in warehouses, which also requires a wide communication range to decrease deployment and human cost.

However, the transmission of electromagnetic signals in space will be affected by weather, such as rainfall, resulting in decreased signal transmission distance. Although the attenuation of rain is relatively tiny in theory, since the wavelength of the 900-MHz wireless signal is 33.33 cm, which is much larger than the diameter of a raindrop, there will still be a small amount of rain attenuation in the actual transmission. Thus, performance verification in various weather conditions remains an essential task for our future work. In addition, future study on the issues with many tags or readers and moving vehicles at high speeds is also necessary for the context of V2I.

References

[1] V.-T. Ta and A. Dvir, "A secure road traffic congestion detection and notification concept based on V2I communications," *Veh. Commun.*, vol. 25, Oct. 2020, Art. no. 100283.

[2] V. Milanes, J. Villagrá, J. Godoy, J. Simó, J. Pérez, and E. Onieva, "An intelligent V2I-based traffic management system," *IEEE Trans. Intell. Transp. Syst.*, vol. 13, no. 1, pp. 49–58, Mar. 2012.

[3] A. R. Khan *et al.*, "Dsrc technology in Vehicle-to-Vehicle (V2V) and Vehicle-to-Infrastructure (v2i) iot system for intelligent transportation system (its): A review," *Recent Trends in Mechatronics Towards Industry 4.0*. Singapore: Springer, 2022, pp. 97–106.

[4] Intell. Transp. Syst. Joint Program Office, Washington, DC, USA. "Dsrc Road Side Unit." Accessed: Nov. 28, 2018. [Online]. Available: https://www.itskrs.its.dot.gov/its/benecost.nsf/ID/3becb13684e99b418525833900698864

[5] U.S. Dept. Transp, Washington, DC, USA. "Dedicated Short-Range Communications Roadside Unit Specifications." Accessed: Apr. 28, 2017. [Online]. Available: https://transops.s3.amazonaws.com/uploaded_files/Dedicated Short Range Communications Roadside Unit Specifications.pdf

[6] Savari. "Road Side Unit." Accessed: Apr. 2017. [Online]. Available: https://www.portlandoregon.gov/transportation/article/691679

[7] M. Liukkonen and T.-N. Tsai, "Toward decentralized intelligence in manufacturing: Recent trends in automatic identification of things," *Int. J. Adv. Manuf. Technol.*, vol. 87, no. 9, pp. 2509–2531, 2016.

[8] Y.-C. Chen, C. N. Chu, R.-S. Chen, H. M. Sun, and P. H. Ju, "RFID-based bonded warehouse for science park," *Int. J. Radio Freq. Identif. Technol. Appl.*, vol. 5, no. 1, pp. 1–23, 2018.

[9] A. K. Biswal, M. Jenamani, and S. K. Kumar, "Warehouse efficiency improvement using rfid in a humanitarian supply chain: Implications for indian food security system," *Transp. Res. Part E Logist. Transp. Rev.*, vol. 109, pp. 205–224, Jan. 2018.

[10] A. Abedi, F. Dehbashi, M. H. Mazaheri, O. Abari, and T. Brecht, "WiTAG: Seamless wifi backscatter communication," in *Proc. Annu. Conf. ACM Spec. Interest Group Data Commun. Appl. Technol. Architect. Protocol. Comput. Commun.*, 2020, pp. 240–252.

[11] Z. Chi, X. Liu, W. Wang, Y. Yao, and T. Zhu, "Leveraging ambient LTE traffic for ubiquitous passive communication," in *Proc. Annu. conf. ACM Spec. Interest Group Data Commun. Appl. Technol. Architect. Protocol. Comput. Commun.*, 2020, pp. 172–185.

[12] V. Liu, A. Parks, V. Talla, S. Gollakota, D. Wetherall, and J. R. Smith, "Ambient backscatter: Wireless communication out of thin air," *ACM SIGCOMM Comput. Commun. Rev.*, vol. 43, no. 4, pp. 39–50, 2013.

[13] X. Tang, G. Xie, and Y. Cui, "Self-sustainable long-range backscattering communication using rf energy harvesting," *IEEE Internet Things J.*, vol. 8, no. 17, pp. 13737–13749, Sep. 2021.

[14] X. Wang, H. Yiğitler, R. Duan, E. Y. Menta, and R. Jäntti, "Coherent multiantenna receiver for BPSK-modulated ambient backscatter tags," *IEEE Internet Things J.*, vol. 9, no. 12, pp. 1197–1211, Jan. 2022.

[15] Y. Zhang, Z. Mou, F. Gao, L. Xing, J. Jiang, and Z. Han, "Hierarchical deep reinforcement learning for backscattering data collection with multiple UAVs," *IEEE Internet Things J.*, vol. 8, no. 5, pp. 3786–3800, Mar. 2021.

[16] J. Wang, J. Zhang, R. Saha, H. Jin, and S. Kumar, "Pushing the range limits of commercial passive RFIDs," in *Proc. 16th {USENIX} Symp. Netw. Syst. Design Implement. ({NSDI})*, 2019, pp. 301–316.

[17] Y. Ma, N. Selby, and F. Adib, "Drone relays for battery-free networks," in *Proc. Conf. ACM Spec. Interest Group Data Commun.*, 2017, pp. 335–347.

[18] A. Varshney, O. Harms, C. Pérez-Penichet, C. Rohner, F. Hermans, and T. Voigt, "Lorea: A backscatter architecture that achieves a long communication range," in *Proc. 15th ACM Conf. Embedded Netw. Sensor Syst.*, 2017, pp. 1–14.

[19] C.-K. Lin, G.-J. Horng, C.-H. Wang, and J.-F. Yang, "Using direction of arrival to detect cognitive traffic sign in city environments," *Wireless Pers. Commun.*, vol. 80, no. 2, pp. 693–708, 2015.

[20] S. Samadi, "Applications and opportunities for radio frequency identification (RFID) technology in intelligent transportation systems: A case study," *Int. J. Inf. Electron. Eng.*, vol. 3, no. 3, pp. 341–345, 2013.

[21] Z. Pala and N. Inanc, "Smart parking applications using RFID technology," in *Proc. 1st Annu. RFID Eurasia*, 2007, pp. 1–3.

[22] H. Tao, M. Zou, and W. Liu, "Optimization management system for level crossing traffic based on rfid," in *Proc. Asia-Pac. Conf. Wearable Comput. Syst.*, 2010, pp. 352–354.

[23] F. M Al-Naima and H. Al-Any, "Vehicle location system based on RFID," in *Proc. Develop. E-Syst. Eng.*, 2011, pp. 473–478.

[24] O. Abari, D. Vasisht, D. Katabi, and A. Chandrakasan, "Caraoke: An e-toll transponder network for smart cities," in *Proc. ACM Conf. Spec. Interest Group Data Commun.*, 2015, pp. 297–310.

[25] S. L. Fong, A. A. A. B. A. Bakar, F. Y. H. Ahmed, and A. Jamal, "Smart transportation system using RFID," In *Proc. 8th Int. Conf. Softw. Comput. Appl.*, 2019, pp. 579–584.

[26] S. Shao, A. Khreishah, and J. Paez, "Passiveretro: Enabling completely passive visible light localization for IoT applications," in *Proc. IEEE INFOCOM Conf. Comput. Commun.*, 2019, pp. 1540–1548.

[27] S. Shao, A. Khreishah, and I. Khalil, "Enabling real-time indoor tracking of IoT devices through visible light retroreflection," *IEEE Trans. Mobile Comput.*, vol. 19, no. 4, pp. 836–851, Apr. 2020.

[28] J. G. D. Hester and M. M. Tentzeris, "Inkjet-printed flexible mm-wave van-atta reflectarrays: A solution for ultralong-range dense multitag and multisensing chipless RFID implementations for iot smart skins," *IEEE Trans. Microw. Theory Techn.*, vol. 64, no. 12, pp. 4763–4773, Dec. 2016.

[29] J. Kimionis, A. Georgiadis, and M. M. Tentzeris, "Millimeter-wave backscatter: A quantum leap for gigabit communication, rf sensing, and wearables," in *Proc. IEEE MTT-S Int. Microw. Symp. (IMS)*, 2017, pp. 812–815.

[30] F. Guidi, N. Decarli, D. Dardari, F. Mani, and R. D'Errico. "Millimeter-wave beamsteering for passive RFID tag localization," *IEEE J. Radio Freq. Identificat.*, vol. 2, no. 1, pp. 9–14, Mar. 2018.

[31] E. Soltanaghaei *et al.*, "Millimetro: mmWave retro-reflective tags for accurate, long range localization," In *Proc. 27th Annu. Int. Conf. Mobile Comput. Netw.*, 2021, pp. 69–82.

[32] M. Katanbaf, A. Weinand, and V. Talla, "Simplifying backscatter deployment: Full-duplex lora backscatter," in *Proc. 18th {USENIX} Symp. Netw. Syst. Design Implement. ({NSDI})*, 2021, pp. 955–972.

[33] Y. Peng *et al.*, "PLoRa: A passive long-range data network from ambient lora transmissions," in *Proc. Conf. ACM Spec. Interest Group Data Commun.*, 2018, pp. 147–160.

[34] F. Amato, C. W. Peterson, M. B. Akbar, and G. D. Durgin, "Long range and low powered RFID tags with tunnel diode," in *Proc. IEEE Int. Conf. RFID Technol. Appl. (RFID-TA)*, 2015, pp. 182–187.

[35] F. Amato and G. D. Durgin, "Tunnel diodes for backscattering communications," in *Proc. 2nd URSI Atlant. Radio Sci. Meeting (AT-RASC)*, 2018, pp. 1–3.

[36] A. Varshney, A. Soleiman, and T. Voigt, "TunnelScatter: Low power communication for sensor tags using tunnel diodes," in *Proc. 25th Annu. Int. Conf. Mobile Comput. Netw.*, 2019, pp. 1–17.

[37] J. D. Griffin and G. D. Durgin, "Complete link budgets for backscatter-radio and RFID systems," *IEEE Antennas Propag. Mag.*, vol. 51, no. 2, pp. 11–25, Apr. 2009.

[38] J. Vandensande, H. Pues, and A. V. de Capelle, "Calculation of the bandwidth of microstrip resonator antennas," in *Proc. 9th Eur. Microw. Conf.*, 1979, pp. 116–119.

[39] Z. N. Chen and M. Y. W. Chia, "Broadband suspended plate antenna with probe-fed strip," *IEE Proc. Microw. Antennas Propag.*, vol. 148, no. 1, pp. 37–40, 2001.

[40] Y.-X. Guo, C.-L. Mak, K.-M. Luk, and K.-F. Lee, "Analysis and design of L-probe proximity fed-patch antennas," *IEEE Trans. Antennas Propag.*, vol. 49, no. 2, pp. 145–149, Feb. 2001.

[41] J. Park, H.-G. Na, and S.-H. Baik, "Design of a modified L-probe fed microstrip patch antenna," *IEEE Antennas Wireless Propag. Lett.*, vol. 3, pp. 117–119, 2004.

[42] R. Garg, P. Bhartia, I. J. Bahl, and A. Ittipiboon, *Microstrip Antenna Design Handbook*. Norwood, MA, USA: Artech House, 2001.

[43] C. Run-Nan, Y. Ming-Chuan, L. Shu, Z. Xing-Qi, Z. Xin-Yue, and L. Xiao-Feng, "Design and analysis of printed yagi-uda antenna and two-element array for wlan applications," *Int. J. Antennas Propag.*, vol. 2012, Oct. 2012, Art. no. 651789. [Online]. Available: https://www.hindawi.com/journals/ijap/2012/651789/

[44] P. Zhang, D. Bharadia, K. Joshi, and S. Katti, "Hitchhike: Practical backscatter using commodity wifi," in *Proc. 14th ACM Conf. Embedded Netw. Sensor Syst. CD-ROM*, 2016, pp. 259–271.

[45] N. Reiskarimian, M. B. Dastjerdi, J. Zhou, and H. Krishnaswamy, "18.2 highly-linear integrated magnetic-free circulator-receiver for full-duplex wireless," in *Proc. IEEE Int. Solid-State Circuits Conf. (ISSCC)*, 2017, pp. 316–317.

[46] V. Badrinarayanan, A. Kendall, and R. Cipolla, "SegNet: A deep convolutional encoder-decoder architecture for image segmentation," *IEEE Trans. Pattern Anal. Mach. Intell.*, vol. 39, no. 12, pp. 2481–2495, Dec. 2017.

[47] B. Sklar. *Digital Communications: Fundamentals and Applications*, vol. 2. Englewood Cliffs, NJ, USA, Prentice-hall, 1988.

[48] RF-Micro-Devices. "MMIC-LNA." Accessed: 2006. [Online]. Available: www.farnell.com/datasheets/1848785.pdf

[49] UIY. "700 to 5000mhz–Coaxial Circulator." Accessed: May 2020. [Online]. Available: https://www.uiy.com/Datasheet/UIYCC2528A.pdf

[50] Microsemi Corporation. "IGLOO Nano Low Power Flash FPGAs." Accessed: Oct. 2015. [Online]. Available: https://www.microsemi.com

[51] Analog Devices. "ADG901/ADG902." Accessed: May 2016. [Online]. Available: https://www.analog.com

[52] Abracon Corporation. "ASTX-H11." Accessed: 2008. [Online]. Available: https://www.abracon.com

[53] Monsoon Solutions. "High Voltage Power Monitor." Accessed: May 2007. [Online]. Available: https://www.msoon.com/high-voltage-power-monitor

[54] F. Perry, K. Raboy, E. Leslie, Z. Huang, and D. V. Duren, "Dedicated short-range communications roadside unit specifications," U.S. Dept. Transp., Saxton Transp. Oper. Lab., McLean, VA, USA, Rep. FHWA-JPO-17-589, 2017.